Tracking oxygen atoms in electrochemical CO oxidation - Part II: Lattice oxygen reactivity in oxides of Pt and Ir

Scott, Søren B.; Kibsgaard, Jakob; Vesborg, Peter C.K.; Chorkendorff, Ib

Published in:
Electrochimica Acta

Link to article, DOI:
10.1016/j.electacta.2021.137844

Publication date:
2021

Document Version
Peer reviewed version

Tracking Oxygen Atoms in Electrochemical CO oxidation - Part II: Lattice Oxygen Reactivity in Oxides of Pt and Ir

Soren B. Scott[a,1], Jakob Kibsgaard[a], Peter C. K. Vesborg[a], Ib Chorkendorff[a,*]

[a] *SurfCat Section for Surface Physics and Catalysis, Department of Physics, Technical University of Denmark, 2800 Kgs Lyngby, Denmark*
[b] *Spectro Inlets A/S, Ole Maaløes Vej 3, 2200 København*

Abstract

Electrochemical oxidation of carbon monoxide (CO oxidation) is often used as a model reaction to investigate the surface of metallic electrocatalysts, most notably in CO stripping experiments. In this report, we use chip-based electrochemistry mass spectrometry with ^{18}O isotope-labeled oxides Pt and Ir to investigate the involvement of lattice oxygen in the electrochemical oxidation of water (the oxygen evolution reaction, OER), adventitious carbon, and CO. For Pt, we find that the labeled oxygen from $Pt^{18}O_x$ is incorporated into the CO_2 resulting from CO oxidation at the potential at which it is reduced to hydroxyl ($*OH$), confirming that $*OH$ is the reactive species in the Langmuir-Hinshelwood electrochemical oxidation of CO. For Ir we find that lattice oxygen in $Ir^{18}O_2$ is similarly involved in electrochemical CO oxidation, but only if it is first activated by a reductive sweep. The labeled CO_2 signal is transient, indicating that activated lattice oxygen provides the "ignition sites" for the Langmuir-Hinshelwood electrochemical oxidation of CO on Ir. We also confirm the previously reported result that electrochemically prepared, amorphous, $Ir^{18}O_x$ incorporates much more lattice oxygen in O_2 evolved during OER than does rutile $Ir^{18}O_2$, but we also quantify the amount and show that in all cases the labeled O_2 is a very small portion of the total O_2 evolved, and that more lattice oxygen is released in CO_2 when oxidizing CO and adventitious carbon than is released in O_2 when oxidizing water. Through these results, we demonstrate that EC-MS in concert with isotope labeling and CO as a probe molecule can provide insight into lattice oxygen reactivity, extending the utility of CO oxidation to the study of noble metal oxides used in *e.g.* PEM electrolyzer anodes.

Keywords: , CO oxidation, oxygen evolution, mass spectrometry, mechanisms

*Corresponding author
Email address: ibchork@fysik.dtu.dk (Ib Chorkendorff)

1. Introduction

Electrocatalysis is at the core of the technologies linking electrical energy and chemical energy, a link which is essential to solve the problems of energy storage and the electrification of chemical industry[1, 2]. Without this link, there is a limit to the extent to which intermittent renewable electricity sources such as wind and solar can replace fossil fuels. The most important of such electrocatalytic processes is water electrolysis to produce hydrogen[3, 4], which can be used as an input to chemical industries such as steel and ammonia production or to regenerate electricity in a hydrogen fuel cell. The most promising technologies in the near- to mid-term for both water electrolyzers[5, 6] and hydrogen fuel cells[7, 8] utilize polymer electrolyte membranes (PEM) to conduct protons from the anode to the cathode, balancing the charge of the electrons flowing through the external circuit and balancing the electrochemical reactions. Noble metal-based catalysts are needed for all four half-reactions taking place at the electrodes of PEM fuel cells and electrolyzers, due to the tendency of non-noble elements to dissolve in the corrosive acidity intrinsic to the polymer electrolyte membrane. Platinum (Pt), a very rare element produced globally in only ∼200 tons per year[9], is used to catalyze the oxygen reduction reaction (ORR) of fuel cell cathodes, the hydrogen oxidation reaction (HOR) of fuel cell anodes, and the hydrogen evolution reaction (HER) of electrolyzer cathodes. Oxides of iridium (Ir), a biproduct of platinum production with only ∼10 tons per year[9], are used to catalyze the oxygen evolution reaction (OER) of electrolyzer anodes. Because of the scarcity of these elements, and the urgent need to scale up PEM technologies, it is more than worthwhile to understand their electrochemical properties in great detail in order to optimize their utilization and in order to gain insight which can aid the design of stable and active electrocatalysts based on more abundant elements.

Carbon monoxide is often used as a probe molecule in electrochemical studies of Pt[10, 11, 12, 13] and Ir[14, 15, 16]. In our first report on tracking oxygen atoms in electrochemical CO oxidation [Scott2020], we confirmed that on Pt, one oxygen atom comes from carbon monoxide and one from the electrolyte, consistent with the Langmuir-Hinshelwood mechanism, by which adsorbed CO ($*$CO) reacts with adsorbed hydroxy ($*$OH). Despite the fact that electrochemical CO oxidation involves *OH adsorption, the initial step of the oxidation of the metal electrode, the reaction has not been of much use in the study of noble metal oxide electrocatalysts such as IrO_x. This is because IrO_x has much smaller reactivity towards *CO than metallic Ir, and its reactivity varies dramatically with small changes in the history and oxidation state of the surface, even controlling for the potential at which the electrode is held when dosing CO[17]. Further complicating matters, to date, the vast majority of studies using CO oxidation have relied on comparing the electrical current in cyclic voltammagrams. On oxide catalysts which have larger capacitance than metal electrodes and often also have pseudocapacitive charging processes, it can be notoriously complex to isolate the charge associated with *CO oxidation[18]. This latter complication, however, can be mitigated by using mass spectrom-

etry (MS) to detect and quantify the product CO_2, and thereby not rely on electrochemical currents alone[13]. MS detection also enables the tracking of atoms in electrocatalytic reactions by isotope labeling.

In this article we study CO oxidation on noble metal oxide surfaces by investigating the interaction of $^{*}CO$ and oxygen species using ^{18}O isotope labeling of the electrode and chip-based electrochemistry - mass spectrometry (EC-MS)[19] to monitor the isotopic distribution of the products in real time. Specifically, we answer the question of whether the *lattice oxygen* from the electrode material plays a role in the reaction, incorporating itself into the CO_2 formed. Here, lattice oxygen can be effectively defined as *oxygen with oxygen-metal bonds which does not reduce to water or exchange spontaneously with oxygen in the electrolyte at any potential anodic of the initial open-circuit potential of the material* [20]. Our question is analogous to the question of whether such lattice oxygen plays a role in oxygen evolution electrocatalysis, one of persistent and growing interest in the field.[21, 22, 23, 24, 25, 26, 27, 28, 29, 30, 31]

We investigate lattice oxygen evolution in the CO oxidation reaction first on an electrochemically formed oxide of platinum, and then three differently-prepared oxides of iridium. Our goal is to develop isotope labeling and electrochemical CO oxidation as a tool to probe the state and reactivity of the oxygen atoms at the catalytic surface of noble metals and noble metal oxides.

2. Experimental

2.1. Samples and electrolytes

- The Pt electrode is a 99.99% polycrystalline Pt stub from MaTeck. It was flame-annealed, cooled in argon, and rinsed in Millipore water before use.
- The Ir samples were prepared from thin films deposited in a sputter chamber (AJA International). Prior to Ir deposition, the glassy carbon substrate was cleaned and a 5 nm Ti sticking layer was sputter deposited. Ir was sputtered from a 99.9% iridium target (Kurt J. Lesker company) with 300 W DC plasma and 5 mTorr Ar in the chamber. The sputtering rate was calibrated with a quartz cyrstal monitor, and 700 s of sputtering was used to deposit 10 nm thick Ir films.
- The overlayer $Pt^{18}O_x$ and $Ir^{18}O_x$ films were produced by electrochemical oxidation of the Pt electrode and metallic Ir film, respectively, in $H_2{}^{18}O$-labeled electrolyte with 50 μA of anodic current for 30 minutes.
- The hydrous $Ir^{18}O_x \cdot yH_2O$ film was prepared by cycling a sputtered Ir film at 50 mV/s from 0 to 1.5 V_{RHE} 100 times.
- The rutile $Ir^{18}O_2$ sample was prepared by reactive sputter deposition with a plasma containing 20% $^{18}O_2$ and 80% Ar. (Further details in Appendix A of ref [20]).

All glassware, as well as the EC cell, were cleaned by soaking overnight in piranha and then boiled in millipore water. Electrolytes were prepared with Millipore H_2O and Suprapur $HClO_4$ (70%) from Sigma-Aldrich. Electrochemical labeling was done in electrolyte prepared from 97% $H_2{}^{18}O$ from Medical Isotopes. Reactive sputtering was done with 99% $^{18}O_2$ from Sigma-Aldrich.

2.2. Electrochemistry - mass spectrometry procedures

The electrochemistry - mass spectrometry (EC-MS) interface was purchased from Spectro Inlets A/S. It centers on a silicon microchip with a perforated silicon membrane. Gaseous products equilibrate across the membrane according to Henry's Law of volatility and are sampled from the chip's internal volume through a capillary to the vacuum chamber containing the quadrupole mass spectrometer. The quadrupole mass spectrometer consisted of a QMA 125 analyzer and QMG electronics system from Pfeiffer Vacuum, and a secondary electron multiplier detector. The setup is described in detail elsewhere [19, 13].

H_2, CO_2, and O_2 were calibrated based on constant-current HER, OER, and COox measurements, respectively. He and CO were calibrated based on the flux through the membrane chip. The reference electrode potential and working distance were calibrated using the open-circuit and transport-limited hydrogen oxidation current, respectively, with H_2 carrier gas. For more details on quantification, see the first article of this series and Section 2.2 of [20].

All experiments were done at 25 °C.

2.3. Determining the isotopic purity of the electrolyte

To determine the isotopic purity of the electrolyte, we measure the MS signals during steady-state oxygen evolution and the equation

$$\alpha = \frac{2}{2+\beta}\,, \tag{1}$$

where $\alpha = \frac{c_{H_2{}^{16}O}}{c_{H_2{}^{16}O}+c_{H_2{}^{18}O}}$ is the fraction ^{16}O in the electorlyte and $\beta = \frac{S_{M34}}{S_{M32}}$ is the measured ratio the signals at m/z=34 to m/z=32. See the SI for the derivation.

β was always measured internally, and α was consistently determined to be between 99.805% and 99.790% and (0.195% to 0.210% ^{18}O). The variation, though slight, is believed to be due to cross-contamination from experiments involving labeled electrolyte, so the cell was dried at 120 °C after experiments involving labeled electrolyte. Another source of isotopic contamination is the isotopic exchange on the walls of the vacuum chamber, especially significant for H_2O (see Ref [20]). For this reason, the vacuum chamber was baked at 100 °C after all experiments involving labeled electrolyte.

Isotope-labeled electrolyte was prepared with water purchased from Medical Isotopes which is 97% $H_2{}^{18}O$. However, it is diluted slightly by addition of the acid (8.6 μl 70% $HClO_4$ per ml).

2.4. Data treatment

The data and analysis and plotting scripts for this work are available at https://github.com/ScottSoren/pyCOox_public. The scripts make use of the open-source `ixdat` python package (https://ixdat.readthedocs.io).

3. Results and Discussion

We present results in this work for platinum and three types of iridium-based electrodes. In each case, we followed the following general procedure:

1. Prepare an electrode with an ^{18}O-labeled oxide at the surface, rinse it with natural water, and dry it.
2. Insert the electrode into unlabelled (99.8% $H_2{}^{16}O$) He-saturated electrolyte and apply 0.25 mA/cm^2 of anodic current until steady state is reached. Observe the isotopic distribution of the O_2 and CO_2 evolved.
3. Lower the electrode potential to a value between the onset of OER and the onset of CO stripping on the corresponding metal (U_{CO}), and hold the potential there while saturating the electrolyte with CO through the chip.
4. Scan the potential in the cathodic direction through U_{CO}. Observe the amount and isotopic distribution of any CO_2 evolved.
   a. If the CO_2 signal increases during the first cathodic scan through U_{CO}, this implies the oxide layer is easily reduced. Continue with cyclic voltammetry over the normal potential range for CO stripping.
   b. If the CO_2 signal stays low during the first cathodic scan through U_{CO}, this implies that the oxide layer is not easily reduced. Reverse the scan to the starting potential and repeat, slowly decreasing the cathodic potential limit until significant CO_2 is evolved. Observe the isotopic distribution of the evolved CO_2.

The isotopes can also be reversed, in which case an un-labeled oxide is made in Step 1 and Steps 2-4 are carried out in labeled electrolyte. In the present work, this reversed isotopic configuration was carried out for Pt (SI) but not the Ir oxides.

Step 2 is included to investigate lattice oxygen involvement in the oxygen evolution reaction before it can be reacted away in the CO oxidation reaction of steps 3 and 4. This also means that any isotopic signal in the CO_2 evolved in these steps implies that the isotopic label survived the OER. Because there is some experimental variability built into the subsequent steps, Step 2 is also the easiest step at which to compare results across sample types (see Section 3.3).

Step 4 is the where the CO oxidation mechanism is probed - and, correspondingly, where CO is used to probe the reactivity of lattice oxygen. In the case that the oxide layer is not reduced during the first cathodic scan (4b), which we observe for the iridium-based oxides, we continued with exploratory experiments to probe the isotopic signals observed.

3.1. CO oxidation on labeled PtO_x

The reactivity of an electrochemically prepared layer of $Pt^{18}O_x$ on Pt is shown in Figure 1. To rule out any artifacts in the measurement, almost-identical experiments are performed for both isotopic configurations: $Pt^{18}O_x$ in $H_2{}^{16}O$ electrolyte (isotopic configuration *A*, Figure 1), and $Pt^{16}O_x$ in $H_2{}^{18}O$ electrolyte (isotopic configuration *B*, described in the SI, Figure S3).

Figure 1a and 1b show the same data plotted in two ways. Each is an EC-MS plot with mass spectrometry signals in the top panel and electrochemical potential and current in the bottom panel with a shared time axis. Figure 1a shows an overview of all of the raw mass spectrometer signals without background subtraction on a logarithmic scale in the top panel. The signals for the carrier gases He at m/z=4 and CO at m/z=28 are also included, providing a clear visualization of the moment at which the carrier gas is switched to saturate the electrolyte with CO. Signals for O_2 at m/z=32, 34, and 36, and for CO_2 at m/z=44, 46, and 48 are clearly visible, as would be expected with or without lattice oxygen involvement due to the natural 0.2% abundance of ^{18}O as well as the fundamental background of the mass spectrometer. The disadvantage of this visualization is that the size and shape of any "isotope signal" implying involvement of lattice oxygen is difficult to discern.

The representation of the data in Figure 1b, on the other hand, makes such isotope signals clear. Here the mass spectrometer signals are calibrated to molecular fluxes as described in the first article of this series, a constant background is subtracted, and the isotopes including ^{18}O are plotted on the left y-axis on a different linear scale from the isotopes containing only ^{16}O, which are plotted on the right y-axis. The axes in the top panel of Figure 1b are scaled according to the natural $^{16}O^{18}O$-to-$^{16}O_2$ ratio of 0.40%, so that $^{16}O^{18}O$ measured at m/z=34 (red trace, left y-axis) and $^{16}O_2$ at m/z=32 (black, right y-axis) coincide when the electrolyte is the only source of oxygen. The natural $C^{16}O^{18}O$-to-$C^{16}O_2$ ratio is also 0.40%, and so $C^{16}O^{18}O$ measured at m/z=46 (purple, left y-axis) and $C^{16}O_2$ at m/z=44 (brown, right y-axis) likewise coincide when the electrolyte is the only source of oxygen. Finally, deviations from this ratio are highlighted: light red for O_2 and light purple for CO_2. **Isotopic signals thus appear as highlighted areas.** The advantage of this method of plotting is that it clearly shows the isotopic signal and, unlike a plot in which data is pre-processed by subtracting a changing background based on the natural isotopic ratio, it makes clear the absolute size of the isotopic signal in relation to the overall signal.

With the plots explained, we look at the experimental data. Starting from the left: first, in He-saturated electrolyte, in unlabeled electrolyte, a constant current of 0.25 mA/cm^2 is applied to the $Pt^{18}O_x$ for five minutes (∼100 to ∼400 s). The total OER production is ≈ 650 pmol/s/cm^2, as expected by Faraday's law of electrolysis: $\dot{n}^{O_2} = {}^{I}/_{4\mathcal{F}}$. The red trace is slightly above the black trace at the start of the 5-minute OER period as plotted in Figure 1b, and this transient excess in m/z=34 is attributed to lattice ^{18}O from the $Pt^{18}O_x$ sample becoming incorporated in the O_2 evolved. The signal for m/z=36 ($^{18}O_2$) is not significantly above the background noise floor. Integrating the excess m/z=34

signal corresponds to 120 pmol/cm^2 excess $^{16}O^{18}O$, or ≈5% of a ML of lattice oxygen. A small excess CO_2 signal labeled with the oxygen from the lattice, $C^{16}O^{18}O$, is also observed, and its size is of a similar magnitude as the isotopic signal in the O_2.

After the 5 minutes of OER, the potential is decreased to 1.3 V_{RHE} and the carrier gas is switched to CO at ∼700 s. Also at the same moment as CO is introduced, a small anodic current rises quickly to a peak of about 15 μA/cm^2 after ≈15 s and then slowly decreases to about 10 μA/cm^2. This anodic current is accompanied by a similarly steady small CO_2 signal dominated by m/z=44.

Finally, starting at ∼1050 s, the potential is cycled down to 0 and then up to 1.4 V_{RHE} at 5 mV/s. The anodic current and the CO_2 signal start increasing slowly, and then a cathodic current wave is closely followed by a peak in CO_2 signal at ∼ 1150 s, when the potential passes the normal onset of CO oxidation on platinum of $U_{CO} \approx 0.75$ V_{RHE}.

The interesting result is the isotopic composition of the CO_2 during this peak, centered at approximately 1150 s. The $C^{16}O^{18}O$ portion increases dramatically from the expected 0.40% to a maximum of 10.5%. This represents a dramatic overproduction (light purple area between the m/z=46 curve and the brown m/z=44 curve in Figure 1b) of the ^{18}O-labeled CO_2 compared not only to the electrolyte isotopic purity, but also compared to the previous OER isotopic distribution.

After this peak, the CO_2 signal drops to near zero as the potential is scanned through the double-layer region. No H_2 is observed at the cathodic potential limit of 0 V_{RHE}, indicating that the surface is poisoned by CO (the m/z=2 signal in Figure 1a is a background signal from water cracking and He double ionization). On the subsequent anodic scan, starting at about 1450 s, there is a dramatic onset of anodic current followed closely by a strong CO_2 signal. This signal, which we attribute to continuous oxidation of CO dissolved in the electrolyte by the now metallic Pt surface, continues through the anodic and subsequent cathodic scan until the potential has returned to below U_{CO}. The purple and brown curves in Figure 1b coincide for this peak, implying that the CO_2 has the natural isotopic distribution.

For isotopic configuration *B* (Figure S3 of the SI), the isotopic distribution of CO_2 f normally favors $C^{16}O^{18}O$. It shows the same effect, with a transient signal during the reductive scan, but at $C^{16}O_2$ instead, as expected based on one ^{16}O from the CO and one from the lattice.

We understand the isotopic signals in these experiments according to the picture sketched in Figure 2 (sketched for isotopic configuration *A*). The experiment starts with an electrochemically grown film of $Pt^{18}O_x$ on top of a metallic Pt bulk in He-saturated natural ($H_2{}^{16}O$) electrolyte. When anodic current is applied in He-saturated electrolyte, the electrolyte is oxidized by the OER to $^{16}O_2$. A very small amount of lattice oxygen enters the O_2 as $^{16}O^{18}O$, but only at the beginning of the OER period, possibly indicating that it arises from certain unstable sites on the $Pt^{18}O_x$ surface which are especially reactive. This transient presumably oxidizes the surface further, "burying" the $Pt^{18}O_x$ under a thin layer of $Pt^{16}O_x$.

When CO is introduced, while holding the potential at 1.3 V_{RHE}, which is anodic of the potential at which Pt can be reduced, only a small amount of CO is oxidized to CO_2, due to the poor activity of PtO_x for CO electro-oxidation. The CO_2 that is produced has oxygen of the natural isotopic distribution, indicating, as might be expected, that the buried labeled oxide is not reactive in the process. However, when the potential is scanned in the cathodic reaction, the surface is slowly reduced. During the reduction, labeled oxygen in the oxide layer is converted to water via $*\,^{18}OH$. According to the Langmuir-Hinshelwood mechanism, $*OH$ is the reactive adsorbate in CO oxidation [10, 11], and so some of it reacts with CO before reducing the rest of the way. The relevant reactions are:

$$*\,^{18}O + (H^+ + e^-) \longrightarrow *\,^{18}OH \tag{2}$$

$$\begin{cases} *\,^{18}OH + (H^+ + e^-) \longrightarrow H_2{}^{18}O + * & (3) \\ *\,^{18}OH + C^{16}O \longrightarrow C^{16}O^{18}O + * + (H^+ + e^-) & (4) \end{cases}$$

The branching coefficient, which partitions ^{18}O between Reactions 3 and 4, is an interesting value, which can be quantified. The total amount of labeled lattice oxygen available for either Reactions 3 or 4 was determined by the reduction in He-saturated electrolyte of an identically prepared sample (Figure S2) to be approximately 5.2 nmol/cm^2. The amount of lattice oxygen that reacts by Reaction 4 for $Pt^{18}O_x$ can be determined by careful analysis of the signals in Figure 1. First, we need to subtract the expected signal due to electrolyte oxidation, which for $C^{16}O^{18}O$ is the $C^{16}O_2$ times the natural isotopic ratio of 0.40%. We need to also correct for the isotopic label lost due to interaction with the electrolyte via $H_2C^{16}O_2{}^{18}O$, the phenomenon described in detail in the first article of this series [Scott2020]. There, we calculate and demonstrate that 22% of the $C^{16}O^{18}O$ produced by $C^{16}O$ oxidation in $H_2{}^{18}O$ electrolyte becomes $C^{18}O_2$. The same ≈20 % loss of the isotopic label can be expected in this experiment, where the isotopes are symmetrically reversed. Figure S4 shows the isotopic signal as a function of potential after subtracting the expected signal due to the impurity of the electrolyte and correcting for the loss of the isotopic label via H_2CO_3.

The integrated isotopic signal after these corrections is 0.80 nmol/cm^2, out of ≈ 5.2 nmol/cm^2 oxide, or 16%, implying branching coefficients for Reaction 4 to Reaction 3 of ≈ 1:5. In other words, most of the ^{18}O ultimately becomes $H_2{}^{18}O$ which is not detected, while we detect the remainder as labeled CO_2. In isotopic configuration *B* (SI), we observe a larger isotope signal, and a branching coefficient closer to 1:2.5. This implies that additional experiments are needed to determine the exact branching coefficient, which is likely highly sensitive to the exact experimental procedures such as scan rate and oxide thickness.

A related insight comes from the maximum portion of $C^{16}O^{18}O$ in the CO_2 produced during the cathodic sweep, here ≈10%. This can be interpreted as the relative rate of CO oxidation and OH formation in the potential range where the the two occur simultaneously. Similar experiments to ours using a constant-potential step rather than a sweep, may be better at determining these relative rates.

3.2. CO oxidation on $Ir^{18}O_x$

In an electrochemical context, metallic iridium behaves very similarly to platinum in its interaction with hydrogen and carbon, but very differently when it comes to oxygen. This can be seen by comparing base cyclic voltammatry and CO oxidation on a metallic Ir film (Figure S1) with those on Pt (Figure 1 of the previous report [Scott2020]). The ignition of CO oxidation is $U_{CO} \approx 0.8$ V_{RHE}, similar to that of Pt. While platinum is a poor OER catalyst, requiring ≈600 mV overpotential for 0.25 mA/cm^2 and forming an increasingly thick inert oxide overlayer during the reaction, iridium requires less than 300 mV overpotential for the same current density (Figure S4). Furthermore, while an oxide film on Pt can be completely reduced in a single cathodic sweep, iridium can form multiple phases of kinetically stable oxides which are much more difficult to reduce [32, 17]. In general, it is more difficult to return an iridium electrode to its "base CV" once it is at all oxidized.

The complexity of iridium's electrochemical interaction with oxygen opens up a huge experimental parameter space, of which this initial report aims to establish isotopically labeled CO oxidation experiments as a probe, but which we can only begin to sample. We show results from investigations in unlabeled electrolyte (0.1 M $HClO_4$ in 99.8% $H_2{}^{16}O$) for three types of labeled iridium samples:

1. A 15 nm thick sputtered rutile $\mathbf{Ir^{18}O_2}$ film, formed by reactive sputtering of Ir in a plasma which is 80% Ar and 20% $^{18}O_2$. This is presented here (Figure 3) and discussed further in the SI (Figures S5 and S6).
2. A thin overlayer of $\mathbf{Ir^{18}O_x}$ formed by constant-current anodization of a 10 nm sputtered metallic iridium film in labeled electrolyte. Based on the analysis in Figure S4, the labeled oxygen incorporated corresponds to ∼1 ML $Ir^{18}O_2$. The electrode was rinsed in un-labeled water before use. These results are presented in the SI (Figure S7).
3. A hydrous $\mathbf{Ir^{18}O_x \cdot yH_2O}$ film formed by potential cycling of a 10 nm sputtered metallic iridium film in labeled electrolyte. The electrode was rinsed in un-labeled water before use. These results are presented in the SI (Figure S8).

All of the results are presented in the same style as Figure 1b in the previous section, with the calibrated mass signals plotted on two axes which are scaled according to the natural isotopic ratio, such that the signature of lattice ^{18}O incorporation in an electrochemical product is a divergence of the $^{16}O^{18}O$ and $^{16}O_2$ traces or of the $C^{16}O^{18}O$ and $C^{16}O_2$ traces. Unlabeled Ir and IrO_2 films were also tested as controls, and show no such isotope signal. The results are compared below in Section 3.3.

Figure 3a shows the O_2 and CO_2 produced by a sputtered film of labeled rutile iridium oxide ($Ir^{18}O_2$) during the start of an extended electrochemical program in un-labeled (99.80% $H_2{}^{16}O$) electrolyte. As in Figure 1, the procedure starts with constant-current oxygen evolution in He-saturated electrolyte. The total O_2 flux and potential quickly stabilize, at 650 $pmol/cm^2/s$ and 1.53 V_{RHE},

respectively. $Ir^{18}O_2$ produces very little CO_2 during this procedure, but the little CO_2 produced does contain an isotopic label, totaling ≈ 80 pmol/cm^2 of lattice ^{18}O in the CO_2 during the 10-minute period after correcting for the isotopic label lost via H_2CO_3. Compared to electrochemically labeled oxides, there is barely any lattice oxygen in the O_2 produced, but integration and careful comparison with an un-labeled control reveals that there is a little bit, about 20 pmol/cm^2 during the 10-minute period, corresponding to 0.005% of the total O_2 produced. In other words, hardly any lattice oxygen is released under OER conditions on rutile iridium oxide. This is consistent with previous results by Mayerhofer and coworkers, who do not observe lattice oxygen in the O_2 produced by sputtered iridium dioxide[31].

At ≈1000 s, the carrier gas is switched from He to CO while the potential is held at 1.0 V_{RHE}. In CO-saturated electrolyte, the potential is cycled with 20 mV/s scans down to a cathodic potential limit and back, with a 1-minute pause at the anodic potential limit each cycle. The reason for this procedure (Step 4b in the general procedure outlined at the start of the Results and Discussion section) is a desire to focus on the "ignition" of CO oxidation which, for a metallic film, corresponds with $*OH$ adsorption, at $\approx U_{CO} = 0.7\,V_{RHE}$. The cathodic excursion reduces the surface of the $Ir^{18}O_2$ film, allowing CO to adsorb, and the pause at the anodic limit is used to observe whether any lattice oxygen is activated by the reduction and then retained to react with CO rather than released as H_2O.

Significant CO_2 production does not occur until after the cathodic limit has been lowered to 0.1 V_{RHE} ($\sim$ 2000 s). The amount of CO_2 then increases with each cycle. This indicates that each subsequent cycle establishes a larger metallic surface overlayer which can bind CO. The isotopic distribution of the CO_2 produced during these cycles is notable. Each potential hold starts with a significant excess of $C^{16}O^{18}O$ (purple areas between the curves) and then approaches, but does not reach, the natural ratio.

Figure 3b shows, starting on the left, a 10-minute potential hold at ($\approx$ 3600 to 4200 s) performed shortly after the procedure shown in Figure 3a. The $C^{16}O^{18}O$ excess can be clearly divided into a transient peaking at about 2.5 pmol/cm^2/s and lasting the first ≈15 s of the potential hold, and a steady portion of about 1 pmol/cm^2/s which lasts the full 10-minute period.

After the 10-minute hold, the electrode is relaxed to open-circuit, and the OCP quickly falls to ≈0.4 V_{RHE}. After that (at ∼4500 s), two cycles are conducted with a 1-minute hold at the anodic potential limit of 0.9 V_{RHE}. The first potential hold, immediately following OCP, has no transient excess of $C^{16}O^{18}O$, and the isotopic distribution goes straight to the steady-state $\approx$ 1 pmol/s/cm^2 excess of $C^{16}O^{18}O$. The second potential hold, following a scan to 0 V_{RHE}, does show a transient. This demonstrates that the reactive ^{18}O that reacts transiently with CO is only formed during the scan down to relatively cathodic potentials.

Figure 4 is a schematic diagram of how we understands the results on rutile $Ir^{18}O_2$. The cycle of activation and reaction of lattice ^{18}O is depicted in the middle portion of Figure 4.

What follows ($\approx$ 4800 to 5900 s, see Figure S6 for the full experiment) is an attempt to "isolate the transient". The potential is scanned to 0 V_{RHE}, but now we decrease the anodic potential limit to only 0.65 V_{RHE} which is just cathodic of the ignition of CO oxidation. With these potential limits the $C^{16}O_2$ production is substantially reduced, but each cycle still produces an excess $C^{16}O^{18}O$ signal peaking on the order of 2 pmol/s/cm^2, indicating a successful isolation of the lattice ^{18}O activating process from conventional Langmuir-Hinshelwood CO oxidation.

After this, continued experimentation (see the SI, Figure S6) indicates that the surface has become increasingly metallic. A CO stripping experiment performed after purging the electrolyte with He further confirms that the surface oxide has been reduced by the procedure in CO-saturated electrolyte. The integrated CO_2 signal in the CO stripping experiment, which contains no isotopic label, corresponds to a roughness factor of approximately 6, indicating significant roughening during the reduction, i.e. the removal of lattice oxygen atoms, from the surface of the $Ir^{18}O_2$ sample (see SI).

The total amount of lattice oxygen evolved in CO_2 during $\approx$ 2 hours experiment of repeated activiation and removal, after correcting for the isotopic label lost via H_2CO_3, is 34 nmol/cm^2, corresponding to $\sim$ 5 ML of flat $Ir^{18}O_2$. We cannot yet determine for this experiment whether additional lattice oxygen was lost as $H_2{}^{18}O$. However, a constant-current OER experiment after the reduction of the surface contained an isotopic label, indicating that at least some labeled oxygen which does not react with CO is accessible, a phenomenon which we do not yet fully understand (See the SI, Figure S6b).

Note that the roughness factor after reduction by CO ($\sim$ 6) is of a similar magnitude to the number of monolayer-equivalents of lattice oxygen previously extracted by CO ($\approx$ 5) as observed in the isotopic signal of the resulting CO_2. This indicates that, in this experiment, *reaction of lattice O with CO is the primary mechanism of reduction and roughening of the surface.*

3.3. Comparison of samples

A theme that is consistent across the experiments for $Pt^{18}O_x$ and all three iridium-based samples (see the SI for electrochemical overlayer $Ir^{18}O_x$ and hydrous $Ir^{18}O_x \cdot yH_2O$) is that CO_2 seems to originate from at least two distinct mechanisms: Langmuir-Hinshelwood oxidation of CO, resulting in the natural isotopic distribution, and a lattice oxygen mechanism, producing CO_2 with an excess abundance of ^{18}O. The Langmuir-Hinshelwood mechanism, when ignited, produces orders of magnitude more CO_2 than does the mechanism involving lattice oxygen, such that the m/z=46 signal due to the natural 0.40% abundance of $C^{16}O^{18}O$ in the Langmuir-Hinshelwood CO_2 is of a similar magnitude to that from the $C^{16}O^{18}O$ resulting from lattice O involvement. The method of plotting used in this report, with two y-axes scaled by the natural isotopic ratio, is essential to simultaneously visualize both processes. It also makes it transparent which background is subtracted when processing the data to isolate the isotopic signal originating in the lattice. We think that it should be standard practice

in isotope-labeling electrocatalysis studies to include this kind of plot, with all the calibrated raw-data plotted on appropriately scaled y-axes.

From these plots, it is clear that the m/z=46 signal is a superposition of the two mechanisms. This is clear during the the 10-minute hold at 0.85 V_{RHE} in Figure 3b during which a $C^{16}O^{18}O$ appears at the beginning of a steady Langmuir-Hinshelwood CO oxidation phase; in Figure S7 ($Ir^{18}O_x$) when the reaction of lattice ^{18}O with CO starts first and then is joined by Langmuir-Hinshelwood CO_2 when the potential is paused at 0.8 V_{RHE}; and when comparing Cycles 1 and 2 in Figure S8 ($Ir^{18}O_x \cdot yH_2O$), where Cycle 2 has more natural CO_2 than Cycle 1, but the two cycles have the same amount and shape of lattice O evolution. Now, we describe these distinct CO_2-producing processes, and then briefly comment on differences between the samples.

The Langmuir-Hinshelwood mechanism for CO_2 oxidation to CO requires, in all cases, a cathodic treatment of the surface followed by an anodic scan passing through $\approx$ 0.7-0.8 V_{RHE}. The cathodic treatment seems, in each case, to require a scan down at least to 0.1 V_{RHE} in CO-saturated electrolyte, though additional cathodic scans increase Langmuir-Hishelwood activity for $Ir^{18}O_2$ and $Ir^{18}O_x \cdot yH_2O$, demonstrating that the first cathodic scan did not fully activate the surface. Our interpretation is that CO can only adsorb to metallic iridium, and thus only at relatively cathodic potentials. Once adsorbed, CO blocks the surface against adsorption of the co-reactant $*OH$ (and thus also blocks further reduction and re-oxidation) until the potential is scanned anodic to the point where the driving force for oxidation of the adsorbed CO is large enough to ignite the reaction.

The lattice oxygen involving mechanism for CO_2 production, on the other hand, is a bit harder to pin down as of yet, and might in fact be multiple distinct mechanisms. Firstly, lattice oxygen is incorporated into the CO_2 produced during the first application of anodic current at the start of each experiment, before the first exposure to CO. This CO_2, which also includes the doubly-labeled $C^{18}O_2$, is believed to originate from hydrocarbon species (adventitious carbon) from air which adsorb by reaction with reactive oxygen atoms at the surface, and is considered separate from lattice oxygen involvement in CO oxidation. In addition, lattice oxygen is incorporated in the CO_2 produced when a labeled iridium oxide electrode is scanned in CO-saturated electrolyte to cathodic potential and back to $>\approx$ 0.6 V_{RHE}. This mechanism is most clearly demonstrated on rutile $Ir^{18}O_2$ in Figure 3. This mechanism produces no $C^{18}O_2$, indicating that it is a non-dissociative CO oxidation mechanism like Langmuir-Hinshelwood. Our explanation is that, at cathodic potentials, the driving force for iridium reduction draws lattice oxygen towards the surface. Some possibly escapes as $H_2{}^{18}O$ (which we cannot detect), but some is trapped at or near the surface as the surface becomes poisoned by CO. These trapped ^{18}O species are then available to react with the adsorbed CO layer when the potential becomes sufficiently anodic. Indeed, this lattice O oxidation is manifested as a m/z=46 transient proceeding or coinciding with the start of $C^{16}O_2$-producing Langmuir-Hinshelwood CO oxidation. Lattice oxygen appears to *ignite* the Langmuir-Hinshelwood oxidation of CO on Ir.

Finally, we briefly remark on the differences between the labeled iridium oxide samples. Each experiment begins with a period of constant-current OER at 0.25 mA/cm^2 in He-saturated electrolyte, and so this part of the experiment is directly comparable. The potential needed to sustain the initial OER current is 1.54 V_{RHE} for rutile $Ir^{18}O_2$, 1.52 V_{RHE} for overlayer $Ir^{18}O_x$, and 1.46 V_{RHE} for hydrous $Ir^{18}O_x \cdot yH_2O$. This ordering of activity is consistent with prior literature on various oxides of Ir[14, 31]. The isotopic distribution of the electrochemical products during electrolysis is summarized in Figure 5. The lattice oxygen incorporation in the O_2 is almost undetectable in rutile $Ir^{18}O_2$ ($\approx$ 20 $pmol/cm^2$ labeled O in O_2 integrated over the 5 minutes), but is easily measurable with this setup in overlayer $Ir^{18}O_x$ ($\approx$ 100 $pmol/cm^2$) and the $^{16}O^{18}O$ signal is much larger still from hydrous $Ir^{18}O_x \cdot yH_2O$ ($\approx$ 700 $pmol/cm^2$). This correlation, by which higher activity is associated with more lattice oxygen incorporation in the evolved O_2, is consistent with prior literature[31]. The isotopic incorporation in the CO_2 evolved during this period, which has not been reported previously to the best of our knowledge, greatly exceeds that of O_2 and follows the same trend, with $Ir^{18}O_2$ ($\approx$ 80 $pmol/cm^2$ labeled O in CO_2 integrated over the 5 minutes) < $Ir^{18}O_x$ ($\approx$ 900 $pmol/cm^2$) < $Ir^{18}O_x \cdot yH_2O$ ($\approx$ 5 $nmol/cm^2$).

4. Conclusion and Outlook

In this work, we used chip-based electrochemistry - mass spectrometry (chip EC-MS) to examine the origin of the oxygen atoms in CO_2 produced by electrochemical oxidation of CO and adventitious carbon on ^{18}O-labeled oxides of platinum and iridium in acidic electrolyte.

We start with oxide overlayers on Pt, which are relatively simple to understand, not least because an oxidized overlayer on platinum can be fully reduced in a single cathodic sweep. Using both isotopic configurations - $Pt^{18}O_x$ in $H_2{}^{16}O$ electrolyte and $Pt^{16}O_x$ in $H_2{}^{18}O$ electrolyte - we show qualitatively identical isotopic effects. Specifically, the isotopic label in the oxygen layer is mostly retained during OER and constant-potential exposure to CO. However, when the potential is scanned in a cathodic direction in CO-saturated electrolyte, a substantial portion of the labeled oxygen is incorporated in CO_2 produced by CO oxidation. This implies a branching during reduction of the oxide, whereby lattice oxygen is activated to $*OH$, and the $*OH$ can be either released as water or react with CO. In the potential-scanning experiments presented here, this branching partitions labeled oxygen between CO_2 and H_2O with a ratio of on the order of 1:2.5 to 1:5. The observation provides new evidence that $*OH$ is the active co-adsorbate in the Langmuir-Hinshelwood mechanism of CO electro-oxidation. Further studies could utilize this method to investigate the kinetics of oxide reduction and CO electro-oxidation on platinum as a function of potential and other conditions.

Finally, we investigate three types of ^{18}O-labeled iridium oxide samples in un-labeled electrolyte. We reproduce the literature result that incorporation of lattice oxygen into O_2 correlates with activity, with rutile IrO_2 < overlayer IrO_x < hydrous $IrO_x \cdot yH_2O$, but show that in each case it is a tiny fraction of the

total O_2 produced. We demonstrate, for the first time, that the incorporation of lattice oxygen in CO_2 produced by the oxidation of adventitious carbon follows the same trend. These observations are consistent with the growing realization that lattice oxygen evolution is in fact a result of high-reactivity, low-stability sites on OER electrocatalysts, which should actually be avoided to improve stability[31]. In each case, the labeled CO_2 signal accounts for more lattice oxygen reaction than the labeled O_2 signal, and so the isotopic distribution of CO_2 produced by an initial anodic scan may be a robust and convenient proxy for its stability.

In CO-saturated electrolyte, we observe an interesting interplay between CO oxidation mechanisms. In all cases, the electrolyte-involving Langmuir-Hinshelwood mechanism is by far the dominant, with lattice oxygen reactivity never exceeding a few pmol/s/cm^2. Although the reaction of lattice oxygen with CO is a secondary route to CO_2, we clearly observe this on rutile iridium dioxide, and the phenomenon turns out to be rather rich. By first performing a cathodic scan lattice oxygen is activated and then incorporated as a transient isotopic label in the CO_2 produced when scanning anodic just before the Langmuir-Hinshelwood CO oxidation mechanism is activated at $\approx$ 0.7 - 0.8 V_{RHE}. Moreover, the same sample supports multiple such transients where lattice oxygen appears in the CO_2 product and only after the equivalent of $\approx$5 ML of oxygen have been released do signs of depletion of the labeled oxygen appear. Thus, we conclude that lattice oxygen can play an important role in igniting the Langmuir-Hinshelwood mechanism on Ir by reacting off the first molecules of adsorbed CO and thus clearing the first sites for adsorption of the reactant $*OH$.

This exploratory report should serve to establish CO oxidation with isotope-labeling and in-situ mass spectrometry as a new tool to investigate the oxide electrocatalysts. We chose to investigate oxides of iridium in acidic electrolyte, because this is the electrocatalytic system of PEM electrolyzer anodes and potentially a major bottleneck in renewable energy storage and utilization due to the scarcity of iridium. Future studies should (1) correlate the reactivity of lattice oxygen in CO oxidation with dissolution of iridium, (2) extract fundamental insight by using CO to probe the reactivity of lattice oxygen on specific single-crystal surfaces of IrO_2, and (3) employ the methods here to investigate the reactivity of lattice oxygen in other oxide electrocatalyst. Ultimately, this may aid the rational design of an abundant replacement for iridium oxide so that water electrolysis can scale up as required.

5. Competing interests

The authors have no competing interests to declare.

6. Acknowledgments

This work was supported by the Villum Foundation VSUSTAIN Grant 9455 to the Villum Center for the Science of Sustainable Fuels and Chemicals.

References

[1] Stefan Lechtenböhmer, Lars J Nilsson, Max Åhman, and Clemens Schneider. Decarbonising the energy intensive basic materials industry through electrification – Implications for future EU electricity demand. *Energy*, 115:1623–1631, 2016.

[2] Zhi Wei Seh, Jakob Kibsgaard, Colin F. Dickens, Ib Chorkendorff, Jens K. Nørskov, and Thomas F. Jaramillo. Combining theory and experiment in electrocatalysis: Insights into materials design. *Science*, 355(6321):eaad4998, jan 2017.

[3] Vojislav R Stamenkovic, Dusan Strmcnik, Pietro P Lopes, and Nenad M Markovic. Energy and fuels from electrochemical interfaces. *Nat Mater*, 16(1):57–69, 2017.

[4] Alessandra Sgobbi, Wouter Nijs, Rocco De Miglio, Alessandro Chiodi, Maurizio Gargiulo, and Christian Thiel. How far away is hydrogen? Its role in the medium and long-term decarbonisation of the European energy system. *International Journal of Hydrogen Energy*, 41(1):19–35, jan 2016.

[5] O Schmidt, A Gambhir, I Staffell, A Hawkes, J Nelson, and S Few. Future cost and performance of water electrolysis: An expert elicitation study. *International Journal of Hydrogen Energy*, 42(52):30470–30492, 2017.

[6] Marcelo Carmo, David L Fritz, Jorgen Mergel, and Detlef Stolten. A comprehensive review on PEM water electrolysis. *International Journal of Hydrogen Energy*, 38(12):4901–4934, 2013.

[7] Hubert A Gasteiger, Shyam S Kocha, Bhaskar Sompalli, and Frederick T Wagner. Activity benchmarks and requirements for Pt, Pt-alloy, and non-Pt oxygen reduction catalysts for PEMFCs. *Applied Catalysis B: Environmental*, 56(1-2 SPEC. ISS.):9–35, mar 2005.

[8] Dustin Banham and Siyu Ye. Current status and future development of catalyst materials and catalyst layers for proton exchange membrane fuel cells: An industrial perspective. *ACS Energy Letters*, 2(3):629–638, 2017.

[9] Peter C K Vesborg and Thomas F Jaramillo. Addressing the terawatt challenge: Scalability in the supply of chemical elements for renewable energy. *RSC Advances*, 2(21):7933–7947, 2012.

[10] K. J.J. Mayrhofer, M. Arenz, B. B. Blizanac, V. Stamenkovic, P. N. Ross, and N. M. Markovic. CO surface electrochemistry on Pt-nanoparticles: A selective review. *Electrochimica Acta*, 50(25-26 SPEC. ISS.):5144–5154, 2005.

[11] Marc T M Koper, Stanley C S Lai, and Enrique Herrero. Mechanisms of the Oxidation of Carbon Monoxide and Small Organic Molecules at Metal Electrodes. *Fuel Cell Catalysis*, pages 159–207, 2009.

[12] Eleonora Zamburlini, Kim D Jensen, Ifan E L Stephens, Ib Chorkendorff, and María Escudero-Escribano. Benchmarking Pt and Pt-lanthanide sputtered thin films for oxygen electroreduction: fabrication and rotating disk electrode measurements. *Electrochimica Acta*, 247:708–721, 2017.

[13] Daniel B. Trimarco, Soren B. Scott, Anil H. Thilsted, Jesper Y. Pan, Thomas Pedersen, Ole Hansen, Ib Chorkendorff, and Peter C.K. Vesborg. Enabling real-time detection of electrochemical desorption phenomena with sub-monolayer sensitivity. *Electrochimica Acta*, 268:520–530, apr 2018.

[14] Tobias Reier, Mehtap Oezaslan, and Peter Strasser. Electrocatalytic Oxygen Evolution Reaction (OER) on Ru, Ir, and Pt Catalysts: A Comparative Study of Nanoparticles and Bulk Materials. *ACS Catalysis*, 2(8):1765–1772, aug 2012.

[15] Julien Durst, Christoph Simon, Frédéric Hasché, and Hubert A Gasteiger. Hydrogen Oxidation and Evolution Reaction Kinetics on Carbon Supported Pt, Ir, Rh, and Pd Electrocatalysts in Acidic Media. *Journal of The Electrochemical Society*, 162(1):F190—-F203, 2015.

[16] Alberto Ganassin, Paula Sebastian, Víctor Climent, Wolfgang Schuhmann, Aliaksandr S Bandarenka, and Juan Feliu. On the pH Dependence of the Potential of Maximum Entropy of Ir(111) Electrodes. *Scientific Reports*, 7(1):1–14, 2017.

[17] Shaun M Alia, Katherine E Hurst, Shyam S Kocha, and Bryan S Pivovar. Mercury underpotential deposition to determine iridium and iridium oxide electrochemical surface areas. *Journal of the Electrochemical Society*, 163(11):F3051—-F3056, 2016.

[18] T Binninger, E Fabbri, R Kötz, and T J Schmidt. Determination of the electrochemically active surface area of metal-oxide supported platinum catalyst. *Journal of the Electrochemical Society*, 161(3), 2014.

[19] Daniel B. Trimarco. *Real-time detection of sub-monolayer desorption phenomena during electrochemical reactions: Instrument development and applications*. Phd thesis, Technical Unviersity of Denmark, 2017.

[20] Soren B Scott. *Isotope-Labeling Studies in Electrocatalysis for Renewable Energy Conversion, and the Net Carbon Impact of this PhD Project*. Phd, Technical University of Denmark, 2019.

[21] J Willsau, O Wolter, and J Heitbaum. In the oxygen evolution reaction on platinum? *Journal of Electroanalytical Chemistry*, 195:299–306, 1985.

[22] M Wohlfahrt-Mehrens and J Heitbaum. Oxygen evolution on Ru and RuO2 electrodes studied using isotope labelling and on-line mass spectrometry. *Journal of Electroanalytical Chemistry*, 237(2):251–260, 1987.

[23] Stéphane Fierro, Tina Nagel, Helmut Baltruschat, and Christos Comninellis. Investigation of the oxygen evolution reaction on Ti/IrO2 electrodes using isotope labelling and on-line mass spectrometry. *Electrochemistry Communications*, 9(8):1969–1974, aug 2007.

[24] Katerina Macounova, Marina Makarova, and Petr Krtil. Oxygen evolution on nanocrystalline RuO2 and Ru0.9Ni0.1O2 electrodes – DEMS approach to reaction mechanism determination. *Electrochemistry Communications*, 11(10):1865–1868, oct 2009.

[25] Yogesh Surendranath, Matthew W Kanan, and Daniel G Nocera. Mechanistic Studies of the Oxygen Evolution Reaction by a Cobalt-Phosphate Catalyst at Neutral pH. *J. Am. Chem. Soc.*, 132(14):16501–16509, 2010.

[26] Oscar Diaz-Morales, Federico Calle-Vallejo, Casper de Munck, and Marc T M Koper. Electrochemical water splitting by gold: evidence for an oxide decomposition mechanism. *Chemical Science*, 4(6):2334, 2013.

[27] Kelsey A Stoerzinger, Oscar Diaz-Morales, Manuel Kolb, Reshma R Rao, Rasmus Frydendal, Liang Qiao, Xiao Renshaw Wang, Niels Bendtsen Halck, Jan Rossmeisl, Heine A Hansen, Tejs Vegge, Ifan E L Stephens, Marc T M Koper, and Yang Shao-Horn. Orientation-Dependent Oxygen Evolution on RuO2 without Lattice Exchange. *ACS Energy Letters*, 2(4):876–881, apr 2017.

[28] Hatem M.A. Amin and H Baltruschat. How many surface atoms in Co3O4 take part in oxygen evolution? Isotope labeling together with differential electrochemical mass spectrometry. *Phys. Chem. Chem. Phys.*, 19:25527–25536, 2017.

[29] Alexis Grimaud, Oscar Diaz-Morales, Binghong Han, Wesley T. Hong, Yueh-Lin Lee, Livia Giordano, Kelsey A. Stoerzinger, Marc T. M. Koper, and Yang Shao-Horn. Activating lattice oxygen redox reactions in metal oxides to catalyse oxygen evolution. *Nature Chemistry*, 9(5):457–465, may 2017.

[30] C Roy, B Sebok, S B Scott, E M Fiordaliso, J E Sørensen, A Bodin, D B Trimarco, C D Damsgaard, P C K Vesborg, O Hansen, I E L Stephens, J Kibsgaard, and I Chorkendorff. Impact of nanoparticle size and lattice oxygen on water oxidation on NiFeOxHy. *Nature Catalysis*, 1(11):820–829, 2018.

[31] Simon Geiger, Olga Kasian, Marc Ledendecker, Enrico Pizzutilo, Andrea M Mingers, Wen Tian Fu, Oscar Diaz-Morales, Zhizhong Li, Tobias Oellers, Luc Fruchter, Alfred Ludwig, Karl J J Mayrhofer, Marc T M Koper, and Serhiy Cherevko. The stability number as a metric for electrocatalyst stability benchmarking. *Nature Catalysis*, 1(7):508–515, 2018.

[32] Lassiné Ouattara, Stéphane Fierro, Olivier Frey, Milena Koudelka, and Christos Comninellis. Electrochemical comparison of IrO2 prepared by anodic oxidation of pure iridium and IrO2 prepared by thermal decomposition of H2IrCl6 precursor solution. *Journal of Applied Electrochemistry*, 39(8):1361–1367, aug 2009.

7. Figures

Figures come at the end, accoring to author guide.

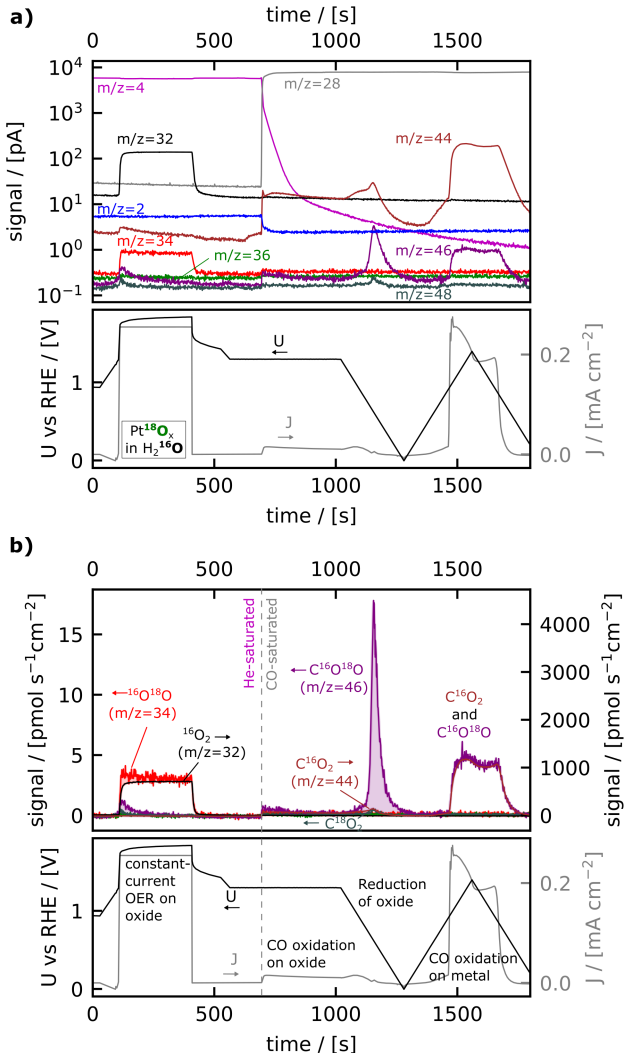

Figure 1: Two representation of the same data from an experiment probing lattice oxygen involvement in OER and CO oxidation on a $Pt^{18}O_x$ overlayer in natural electrolyte (0.1 M $HClO_4$ in 99.80% $H_2{}^{16}O$). In **(a)**, raw mass spectrometer (MS) signals are plotted in the upper panel on a single logarithmic scale. The electrochemical potential and current are plotted in the lower panel. In **(b)**, MS signals are calibrated and plotted on two linear axes, with ^{18}O-containing species on the left y-axis and others on the right y-axis. The two y-axes are scaled such that the traces for $(C)^{16}O^{18}O$ and $(C)^{16}O_2$ coincide when the product has the natural isotopic distribution. Deviations from this ratio are highlighted. The lower panel is annotated with interpretations of the data. The experiment is started in He-saturated electrolyte, and CO is introduced at ∼700 s.

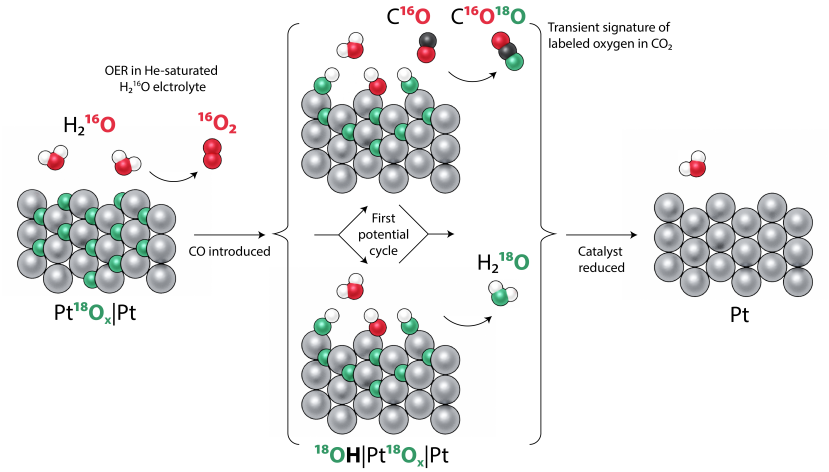

Figure 2: Sketch of experiment probing the reactivity of lattice oxygen on platinum with OER and CO oxidation. The left panel shows the starting point where oxygen in the platinum oxide is ^{18}O and the electrode is performing OER in unlabled water resulting (essentially) only in unlabelled O_2 (around the 100 s to 400 s mark in figure 1). The middle panel is the transient situation in which the electrode is supplied with CO and the potential is scanned down to where $*OH$ groups appear on the surface (around the 1100 s to 1200 s mark in figure 1). Under these conditions the electrode supplies ^{18}O to form $C^{16}O^{18}O$, as well as $H_2{}^{18}O$ which is not directly detected. The right panel shows that after the transient reduction the surfaces is reduced to metallic platinum.

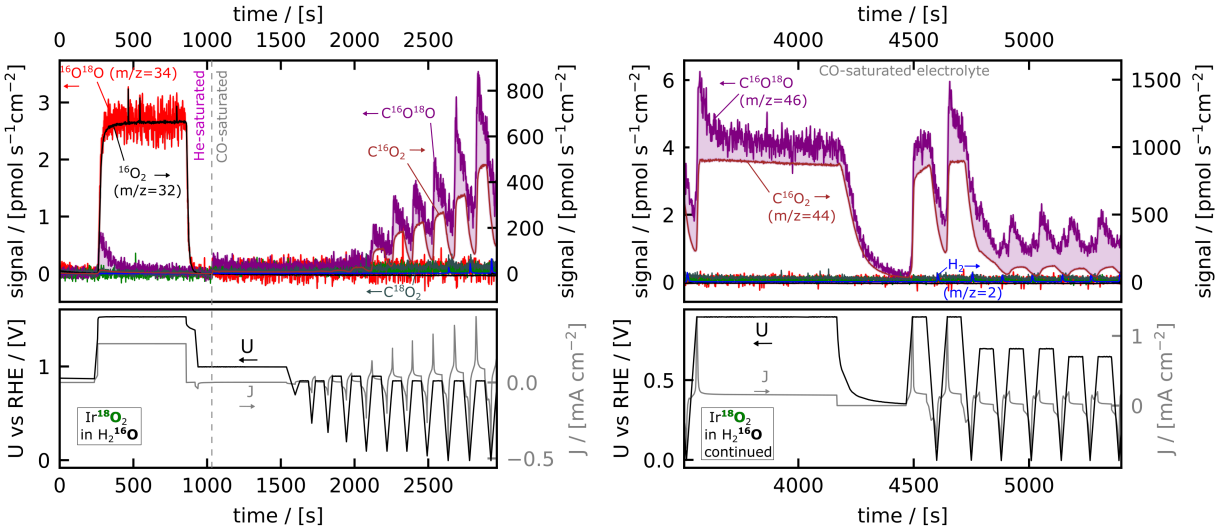

Figure 3: Lattice oxygen involvement in electrochemical CO oxidation on sputter deposited $Ir^{18}O_2$. Two parts of an extended experiment are shown as EC-MS plots with the calibrated signals for ^{18}O-containing isotopes on plotted on the top left y-axis and other calibrated signals plotted on the right y-axis. The two axes are scaled according to the natural $^{16}O^{18}O$-to-$^{16}O_2$ ratio. Excesses of the ^{18}O-containing signals are highlighted. **(a)** Constant-current electrolysis in He-saturated electrolyte followed by potential cycling, with pauses at various anodic potential limits, in CO-saturated electrolyte. **(b)** A varied potential cycling program probing the isotopically labeled CO2 evolved in CO-saturated electrolyte. First, a long pause in CO-saturated electrolyte showing the initial isotope-labeled transient. See Figure SX for the full experiment. All together, the integrated $C^{16}O^{18}O$ signal exceeds that expected by the natural isotopic ratio by 7.8 nmol/cm^2, implying an average of $\sim$ 1/300 CO_2 molecules carries an oxygen atom from the electrode lattice.

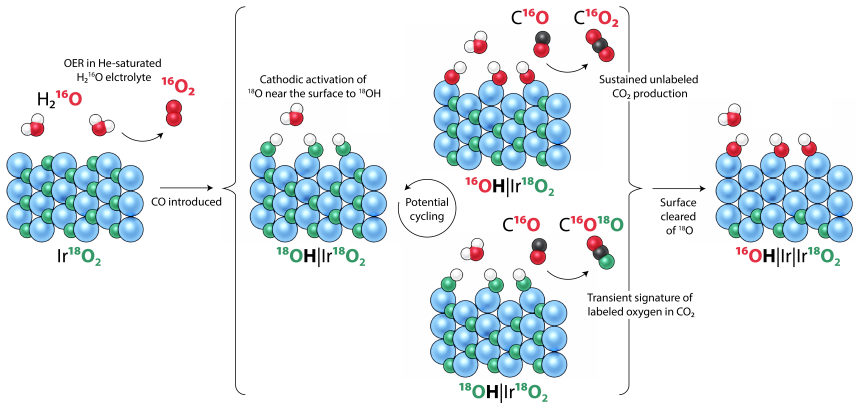

Figure 4: Sketch of experiment probing the reactivity of lattice oxygen in iridium oxide with OER and CO oxidation. The left panel shows the starting point where oxygen in the iridium oxide is ^{18}O and the electrode is performing OER in unlabled water making almost exclusively unlabeled O_2 (around the 300 s to 800 s mark in figure 3a). The middle panel shows the repeated potential cycling under a $C^{16}O$ saturated conditions (the 2000 s to 7500 s mark in figure 3a). During this time the electrode produces mostly unlabeled CO_2 (2531 nmol/cm^2), but also substantially more labeled $C^{16}O^{18}O$ than can be explained by the isotopic impurity of the electrolyte and feed CO. The right panel shows that the iridium surface reduces to metallic form, but that ^{18}O remains burried in the sample.

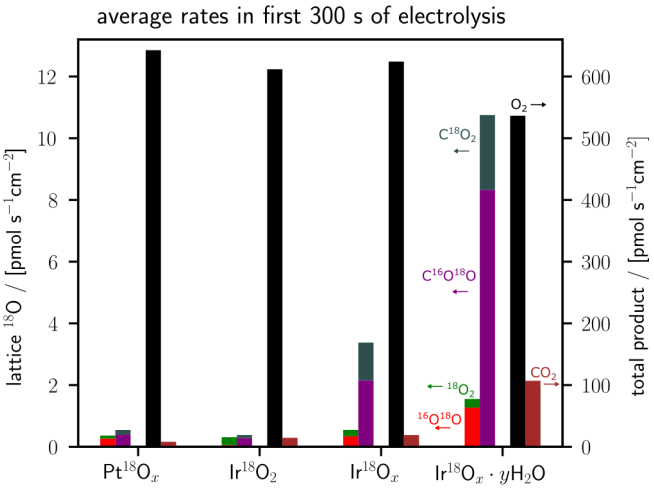

Figure 5: Summary of lattice oxygen involvement during the first five minutes of constant-current electrolysis on four samples. The rate of lattice oxygen evolved as each indicated species, averaged over five minutes of electrolysis, is plotted on the left y-axis and the total O_2 and CO_2 is plotted on the right y-axis. All are divided by the electrolysis time. The scale of the axes is 1:50, such that equal height of bars would indicate that one lattice oxygen atom is included for every 50 molecules of product.